



## Transmembrane helices mediate the formation of a stable ternary complex of b<sub>5</sub>R, cyt b<sub>5</sub>, and SCD1

Jiemin Shen <sup>1</sup>, Gang Wu<sup>2</sup>, Ah-Lim Tsai<sup>2</sup> & Ming Zhou <sup>1</sup>✉

Mammalian cytochrome b<sub>5</sub> (cyt b<sub>5</sub>) and cytochrome b<sub>5</sub> reductase (b<sub>5</sub>R) are electron carrier proteins for membrane-embedded oxidoreductases. Both b<sub>5</sub>R and cyt b<sub>5</sub> have a cytosolic domain and a single transmembrane (TM) helix. The cytosolic domains of b<sub>5</sub>R and cyt b<sub>5</sub> contain cofactors required for electron transfer, but it is not clear if the TM helix has function beyond being an anchor to the membrane. Here we show that b<sub>5</sub>R and cyt b<sub>5</sub> form a stable binary complex, and so do cyt b<sub>5</sub> and stearyl-CoA desaturase-1 (SCD1). We also show that b<sub>5</sub>R, cyt b<sub>5</sub> and SCD1 form a stable ternary complex. We demonstrate that the TM helices are required for the assembly of stable binary and ternary complexes where electron transfer rates are greatly enhanced. These results reveal a role of the TM helix in cyt b<sub>5</sub> and b<sub>5</sub>R, and suggest that an electron transport chain composed of a stable ternary complex may be a general feature in membrane-embedded oxidoreductases that require cyt b<sub>5</sub> and b<sub>5</sub>R.

<sup>1</sup>Verna and Marrs McLean Department of Biochemistry and Molecular Biology, Baylor College of Medicine, Houston, TX 77030, USA. <sup>2</sup>Division of Hematology-Oncology, University of Texas McGovern Medical School, Houston, TX 77030, USA. ✉email: [mzhou@bcm.edu](mailto:mzhou@bcm.edu)

Cytochrome  $b_5$  (cyt  $b_5$ ) and cytochrome  $b_5$  reductase ( $b_5R$ ) are obligatory partners for a number of membrane-embedded oxidoreductases such as fatty acid desaturases and elongases, oxygenases, and cytochrome P450s (cyt P450)<sup>1,2</sup>.  $b_5R$  and cyt  $b_5$  form part of an electron transport chain that transfers electrons from a reductant, nicotinamide dinucleotide (NADH) or nicotinamide dinucleotide phosphate (NADPH), first to the flavin adenine dinucleotide (FAD) cofactor of  $b_5R$ <sup>3</sup>, then the heme moiety of cyt  $b_5$ <sup>4</sup> and finally the metal ions in the catalytic center of the membrane-embedded oxidoreductases.

Mammalian stearoyl CoA desaturase-1 (SCD1) is a membrane-embedded oxidoreductase that catalyzes the formation of the first double-bond in saturated fatty acids. SCD1 has a major role in the regulation of fatty acid metabolism and membrane synthesis and is a validated drug target for many types of cancers<sup>5–8</sup>, neurodegenerative diseases<sup>9–11</sup>, and metabolic diseases<sup>12–15</sup>. The double-bond formation is catalyzed by a diiron center in SCD1, which requires electrons from NAD(P)H delivered by  $b_5R$  and cyt  $b_5$  (Fig. 1).

Extensive structural and functional studies have been conducted on the soluble forms of  $b_5R$  and cyt  $b_5$  that lack their transmembrane (TM) domains. These studies show that the soluble domains of  $b_5R$  and cyt  $b_5$  are sufficient to support electron transfer, and that charged residues on the surface of the soluble domains mediate their interactions<sup>16–21</sup>. However, less attention has been paid to the role of their TM domains, and a stable cyt  $b_5$ - $b_5R$  binary complex has not been isolated.

Studies of SCD1 have shown that  $b_5R$  and cyt  $b_5$  are required for the activity of SCD1<sup>12,22–24</sup>. Whether cyt  $b_5$  and SCD1 form a stable complex via interactions in their TM domains and whether such a stable complex enhances the activity of SCD1 have not been explored. These questions are important in terms of understanding how each redox component of the electron transport chain function in the native environment and the mechanisms of electron transfer. Knowledge on stable binary or ternary complexes of electron transfer partners is relevant in developing novel strategies to inhibit SCD1 or other membrane-bound oxidoreductases.

## Results

**Colocalization and formation of stable binary and ternary complexes in cells.** We first examined the colocalization of SCD1, cyt  $b_5$ , and  $b_5R$  in cells. We fused mouse SCD1 with a green fluorescent protein (GFP), mouse cyt  $b_5$  with a Myc tag, and mouse  $b_5R$  with a hemagglutinin (HA) tag, and monitored the cellular localization of the three proteins by immunofluorescence confocal microscopy. When SCD1 was expressed, a meshwork-like distribution of GFP fluorescence was observed (Supplementary Fig. 1a–f), consistent with its localization to the endoplasmic reticulum (ER) membranes<sup>25</sup>. Cells co-expressing SCD1 and cyt  $b_5$  exhibited overlapping fluorescence, and although the fluorescence from cyt  $b_5$  clustered with most of that from SCD1 as shown in yellow in the merged image (Fig. 2a), cyt  $b_5$  seemed to have a wider distribution than SCD1 likely due to different expression levels of these proteins and participation of cyt  $b_5$  in

multiple redox pathways. Colocalization was also evident in cells co-expressing cyt  $b_5$  and  $b_5R$  (Fig. 2b), consistent with their roles in mediating electron transfer to redox enzymes. Co-localization of all three proteins was observed when the three were co-expressed in the same cells (Fig. 2c). These observations led us to further examine if cyt  $b_5$  form stable binary complexes with  $b_5R$  or SCD1 and if the three form a stable ternary complex.

To test whether the proximity in their expression patterns leads to the formation of stable binary or ternary complexes, we next examined their interactions by co-immunoprecipitation (co-IP). We found that cyt  $b_5$  co-immunoprecipitates with SCD1,  $b_5R$  with cyt  $b_5$ , and  $b_5R$  and cyt  $b_5$  with SCD1 (Fig. 2f–g). We also generated binary fusions by connecting SCD1 and cyt  $b_5$ , and cyt  $b_5$  and  $b_5R$  to test their assembly with  $b_5R$  or SCD1, respectively. The SCD1-cyt  $b_5$  fusion protein has a C-terminal GFP tag, and cyt  $b_5$ - $b_5R$  fusion protein has an N-terminal Myc tag. Colocalization analysis showed that SCD1 and cyt  $b_5$ - $b_5R$  (Fig. 2d), SCD1-cyt  $b_5$  and  $b_5R$  (Fig. 2e) are in close proximity in cells. Co-IP results indicate that the binary fusions led to higher level of the ternary complex than co-expression of SCD1, cyt  $b_5$ , and  $b_5R$  (Fig. 2h–i).

**Stable binary complex between  $b_5R$  and cyt  $b_5$ .** We proceeded to the large-scale production of cyt  $b_5$  and  $b_5R$  complex for further biochemical characterizations. However, simply co-expressing the full-length cyt  $b_5$  and  $b_5R$  did not produce sufficient amount of complex. To increase the yield of the stable complex, and encouraged by previous reports on the production of stable dimeric membrane proteins after fusing two monomers<sup>26–28</sup>, we adopted the strategy of expressing a fusion protein of full-length cyt  $b_5$  and  $b_5R$  as a concatenated chimera with a linker connecting the C-terminus of cyt  $b_5$  to the N-terminus of  $b_5R$  (Fig. 3a). The linker contained a tobacco etch virus (TEV) protease recognition site and can be cleaved after purification. The fusion protein was expressed and purified, and the yield was sufficient for further biochemical studies (Fig. 3b). The fusion protein contains a heme, as indicated by the UV/Vis absorption spectrum (Fig. 3b), and elutes as a single peak on a size-exclusion chromatography (SEC) column. After the linker was cleaved by the TEV protease, cyt  $b_5$  and  $b_5R$  stayed together as a stable complex as indicated by the same elution volume as that of the fusion protein (Fig. 3b). However, when the soluble domains of cyt  $b_5$  and  $b_5R$  were expressed as a fusion protein, the two soluble domains did not stay as a stable complex after cleavage of the linker (Supplementary Fig. 3a, d). These results indicate that interactions between the TM domains are required to maintain the stable binary complex.

We next measured the rate of electron transfer in the stable binary complex of cyt  $b_5$  and  $b_5R$ . We measured the reduction of cyt  $b_5$  in the context of a stable complex with  $b_5R$  or as an individual protein mixed with  $b_5R$ . We found that the time course of cyt  $b_5$  reduction can be fit with a biphasic exponential function ( $k_1$  and  $k_2$ ) when cyt  $b_5$  and  $b_5R$  were in a stable binary complex (Supplementary Fig. 2a). The biphasic kinetics of electron transfer was also observed in the soluble fusion of cyt  $b_5$ - $b_5R$  with similar rates to those of the full-length fusion. In contrast, the time

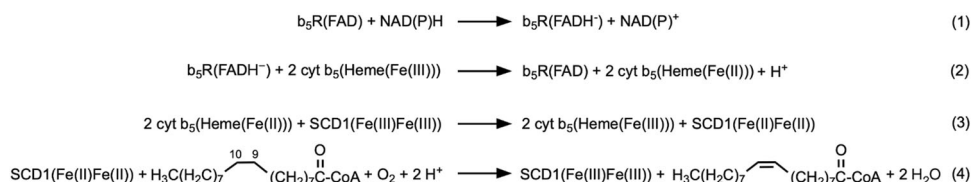


**Fig. 1 Stepwise reactions in the electron transport chain of  $b_5R$ , cyt  $b_5$ , and SCD1.** The redox states of cofactors in proteins are indicated in the parentheses.

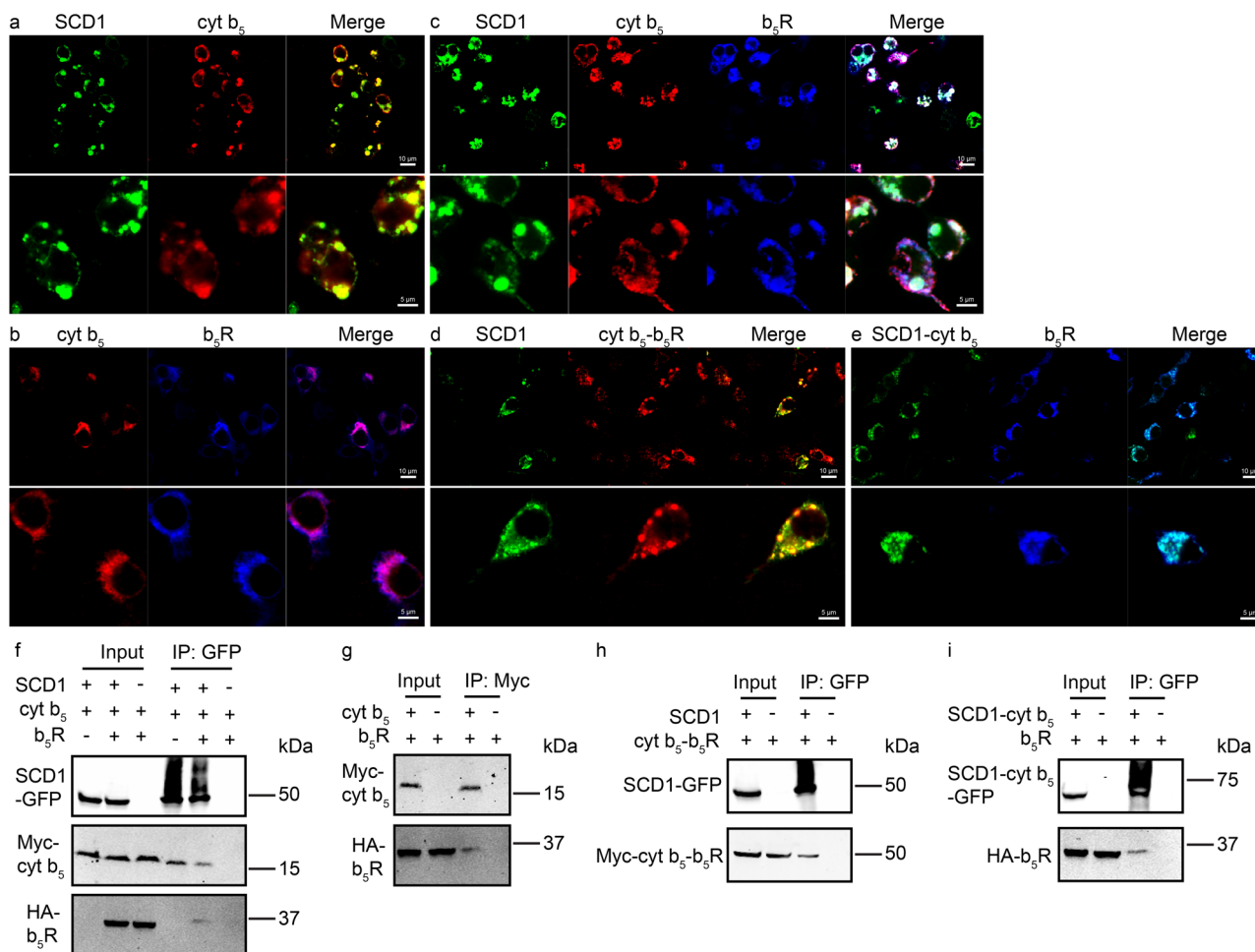


**Fig. 2 Colocalization and co-immunoprecipitation (co-IP) of SCD1, cyt b<sub>5</sub>, b<sub>5</sub>R, and their binary fusions.** Confocal microscopy images show the subcellular distribution and colocalization of **a** SCD1-GFP (green) and Myc-cyt b<sub>5</sub> (red); **b** Myc-cyt b<sub>5</sub> (red) and HA-b<sub>5</sub>R (blue); **c** SCD1-GFP (green), Myc-cyt b<sub>5</sub> (red), and HA-b<sub>5</sub>R (blue); **d** SCD1-GFP (green) and Myc-cyt b<sub>5</sub>-b<sub>5</sub>R (red); **e** SCD1-cyt b<sub>5</sub>-GFP (green) and HA-b<sub>5</sub>R (blue). **a–e** Images in the top and bottom panels are from the same samples of different magnifications. White scale bars represent 10 μm for the top panels and 5 μm for the bottom panels. **f** Co-IP of SCD1, cyt b<sub>5</sub>, and b<sub>5</sub>R. Cells co-expressing SCD1-GFP and Myc-cyt b<sub>5</sub> (left lane) were solubilized, and the lysate was immunoprecipitated with GFP nanobody-conjugated resins. Detection of Myc-cyt b<sub>5</sub> after extensive wash of the resins indicates some stable complex assembly between SCD1 and cyt b<sub>5</sub>. Similarly, ternary complex formation was demonstrated from cells co-expressing tagged SCD1, cyt b<sub>5</sub>, and b<sub>5</sub>R (middle lanes). The lysate from cells expressing tagged cyt b<sub>5</sub> and b<sub>5</sub>R (right lane) served as a negative control to exclude the possibility of non-specific binding of cyt b<sub>5</sub> and b<sub>5</sub>R to resins and non-specificity of antibodies used in western blots. **g** Co-IP of cyt b<sub>5</sub> and b<sub>5</sub>R shows the existence of some stable cyt b<sub>5</sub>-b<sub>5</sub>R complex. Unlike in **f**, lysates were immunoprecipitated with anti-Myc antibodies and protein A resins to capture Myc-cyt b<sub>5</sub>. **h** Co-IP of SCD1 with the binary fusion of cyt b<sub>5</sub>-b<sub>5</sub>R. **i** Co-IP of the binary fusion of SCD1-cyt b<sub>5</sub> with b<sub>5</sub>R. For all the input lanes, 6% of cell lysate was loaded. IP, immunoprecipitation. All the data are from one representative experiment of at least two independent repeats.

course can be fitted with a single exponential function when the soluble forms of individual cyt b<sub>5</sub> and b<sub>5</sub>R were mixed (Supplementary Fig. 2b). The electron transfer rate ( $k_1$ ) is ~34-fold faster in the stable binary complex than that in the mixture of individual proteins in 150 mM NaCl. Thus, the formation of a stable cyt b<sub>5</sub>-b<sub>5</sub>R complex enhances the spatial proximity and the precise alignment of the two soluble domains to facilitate electron transport.

The rate of electron transfer between soluble forms of b<sub>5</sub>R and cyt b<sub>5</sub> is known to be sensitive to ionic strength<sup>29</sup>. We next tested how the ionic strength affects the rate of electron transfer from b<sub>5</sub>R to cyt b<sub>5</sub> in the stable complex. The time courses of cyt b<sub>5</sub> reduction in the stable binary complex and the mixture of two individual proteins were followed in buffer with different NaCl concentrations, and the rates were calculated from either double exponential fitting for the fusion proteins or single exponential fitting for the mixture of individual proteins. The full-length and

soluble fusions displayed a similar trend of ionic strength dependence where the electron transfer rates ( $k_1$  and  $k_2$ ) peaked at ~50 mM NaCl and decreased as [NaCl] increased (Fig. 3c). When the two proteins form a stable binary complex, the difference between no NaCl and 150 mM NaCl is only 1.04-fold. However, when the two proteins were not assembled as a stable complex, ionic strength has a significant effect on the rate of electron transfer (Fig. 3d): an ~8-fold decrease was observed from no NaCl to 150 mM NaCl. These results suggest that the formation of a stable binary complex aligns the soluble domains in position for electron transfer so that electrostatic interactions have a much smaller role in guiding and facilitating the proper interactions of the soluble domains.

**Stable binary complex between cyt b<sub>5</sub> and SCD1.** We next investigated whether the full-length cyt b<sub>5</sub> forms a stable complex with SCD1. We found that co-expression of the two proteins does

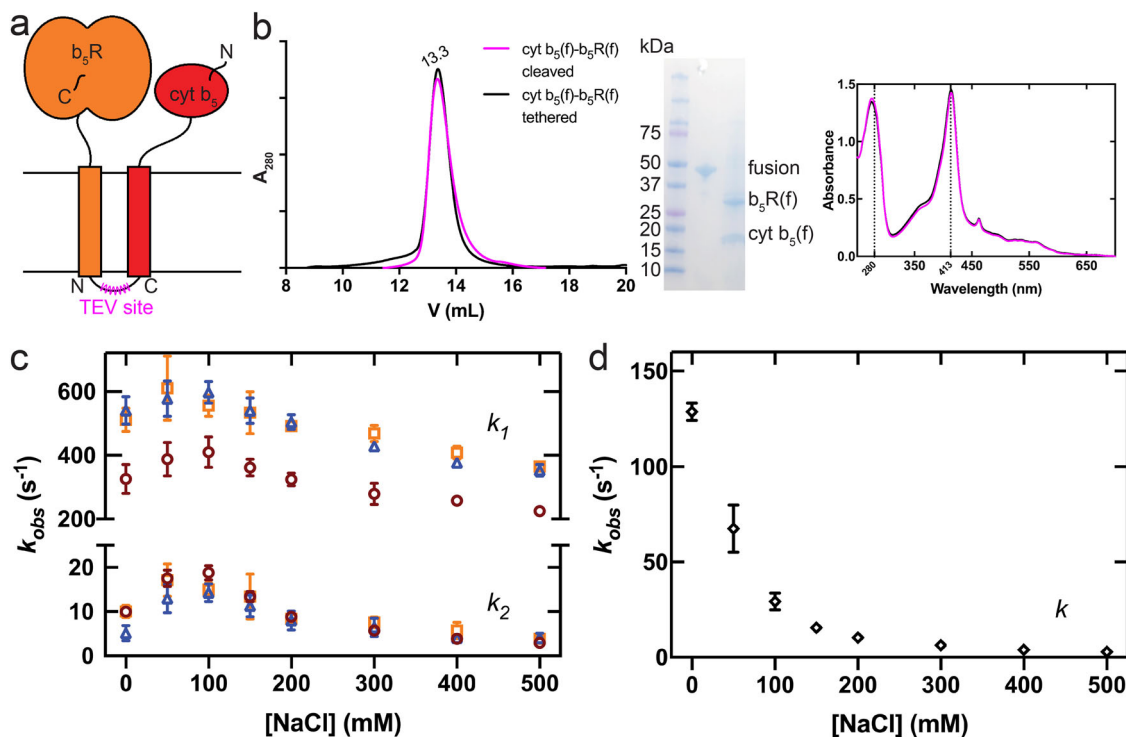


**Fig. 3 Full-length cyt  $b_5$  and full-length  $b_5R$  can form a stable complex with faster electron transfer kinetics.** **a** Schematic diagram of cyt  $b_5$ - $b_5R$  fusion constructs. The N and C denote the N-terminus and C-terminus of cyt  $b_5$  and  $b_5R$ . The magenta zigzag line indicates the placement of a TEV protease site on the linker region connecting the cyt  $b_5$  and  $b_5R$ . **b** Size-exclusion chromatography (SEC) profile (left), SDS-PAGE image (inset), and UV-Vis spectra (right) of the linker-cleaved (magenta) and tethered (black) fusion of SCD1-cyt  $b_5$ . Almost identical SEC profiles and optical spectra suggest the stable assembly between full-length cyt  $b_5$  and  $b_5R$ . **c** Ionic strength-dependent electron transfer in different constructs of cyt  $b_5$ - $b_5R$ : linker-cleaved full-length (orange); tethered full-length (blue); tethered soluble without TM domains (red). The upper and lower half of the plot represent the rate constants of the fast phase ( $k_1$ ) and the slow phase ( $k_2$ ), respectively. **d** Ionic strength-dependent electron transfer between individual  $b_5R$  and cyt  $b_5$ . Different from those of cyt  $b_5$ - $b_5R$  fusions, the time courses with individual  $b_5R$  and cyt  $b_5$  are monophasic. Error bars represent standard error of the mean (SEM) from three independent repeats ( $n = 3$ ).

not produce a high level of stable SCD1-cyt  $b_5$  binary complex. We then applied the fusion protein strategy and linked the C-terminus of SCD1 to the N-terminus of the full-length cyt  $b_5$  with a TEV recognition site in the linker (Fig. 4a). The SCD1-cyt  $b_5$  fusion protein had a sufficient yield and eluted as a single peak on a SEC column (Fig. 4b). After cleavage of the linker, SCD1 and cyt  $b_5$  stayed together as a stable complex as indicated by the single peak on a SEC column; the UV-Vis spectra of the elution peaks are identical before and after TEV protease treatment (Fig. 4b). When the soluble domain of cyt  $b_5$  was fused to SCD1, the two did not stay together as a stable complex after the linker was cleaved, as indicated by two peaks on a SEC column (Supplementary Fig. 3b, e), indicating that the TM domain of cyt  $b_5$  is required for the formation of the stable binary complex.

We then examined if the stable binary complex of SCD1-cyt  $b_5$  is capable of receiving electrons from  $b_5R$ , and transferring electrons from cyt  $b_5$  to SCD1. We first measured the enzymatic activity of SCD1-cyt  $b_5$  by including  $b_5R$  and NADH, and we monitored the reaction by following the consumption of NADH in the presence and absence of a substrate stearyl-CoA. As shown in Fig. 4c, the fast-phase rate of NADH consumption is 1000-fold faster than the rate in the absence of stearyl-CoA. Next, we measured individual electron transfer steps by following the optical change of cyt  $b_5$ . The reduced form of cyt  $b_5$  was monitored by its Soret peak at 423 nm. Under the anaerobic condition, cyt  $b_5$  in the stable binary complex of SCD1-cyt  $b_5$  was first reduced by  $b_5R$  after equimolar of NADH was added, corresponding to the fast-rising phase (Fig. 4d,  $t < 20$  s). After the exhaustion of NADH, the phase of re-oxidation ( $t > 20$  s) of cyt  $b_5$

by SCD1 appeared. The electron transfer rate between cyt  $b_5$  and SCD1 in the stable binary complex is  $7.3 \pm 0.7 \times 10^{-2} \text{ s}^{-1}$ , almost 10-fold higher than that in the mixture of individual cyt  $b_5$  and SCD1 (Fig. 4d). These results indicate that the stable binary complex of SCD1 and cyt  $b_5$  is fully functional, and that the formation of the stable binary complex likely facilitates the alignment and interactions of the two proteins inductive to electron transfer.

#### Stable ternary complex between $b_5R$ , cyt $b_5$ , and SCD1.

Encouraged by the biochemical isolation of the two stable binary complexes, we attempted the production of a stable ternary complex of SCD1, cyt  $b_5$  and  $b_5R$ . We took a similar strategy of connecting all three full-length proteins with TEV protease-cleavable linkers as shown in Fig. 5a. The purified fusion protein eluted as a single peak from a SEC column (Fig. 5b). After the linkers were cleaved, all three proteins stayed together as a stable ternary complex (Fig. 5b). Similarly with results from the binary complexes, SCD1 does not stay together with soluble cyt  $b_5$  and  $b_5R$  in SEC (Supplementary Fig. 3c, f).

The stable ternary complex is fully functional, as indicated by the production of oleoyl-CoA when supplied with NADH and stearyl-CoA (Fig. 5c). The rate of oleoyl-CoA production is significantly faster than those in individual proteins or the stable SCD1-cyt  $b_5$  binary complex (Fig. 5d), indicating that the stable ternary complex forms an efficient electron transport chain and enhances the alignment of electron donors and acceptors. When the stable ternary complex is reconstituted into liposomes



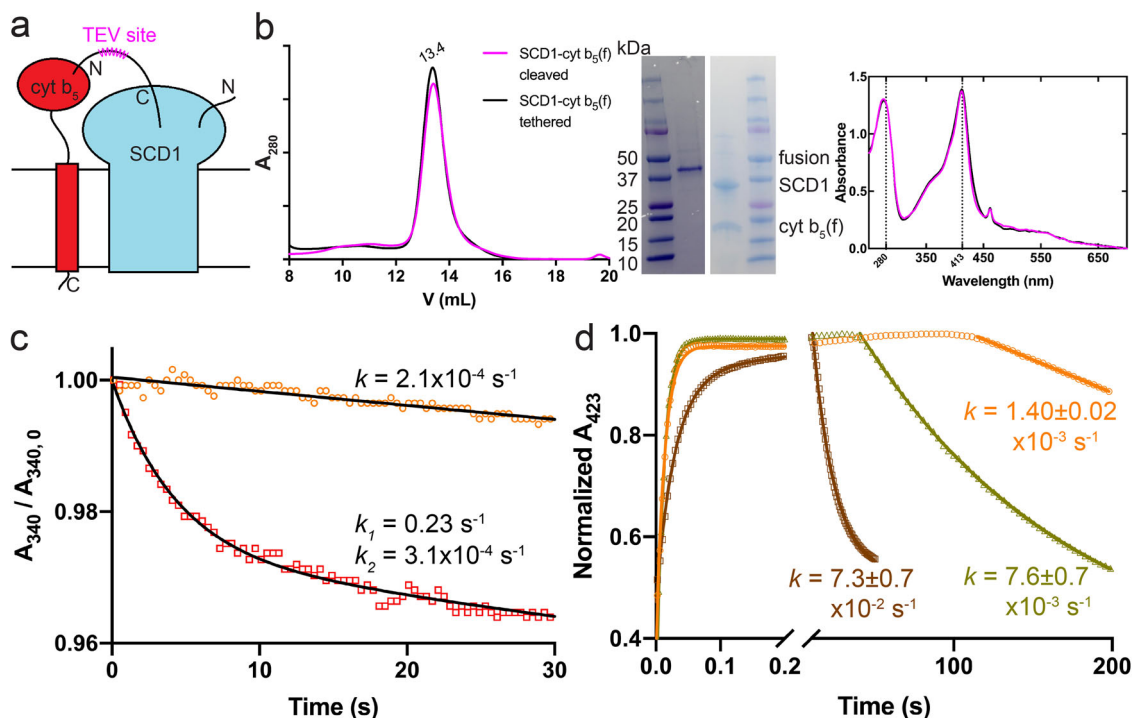


**Fig. 4** SCD1 and full-length cyt b5 can form a stable complex with faster electron transfer kinetics. **a** Schematic diagram of SCD1-cyt b5 fusion constructs. **b** SEC profile (left), SDS-PAGE image (inset), and UV-Vis spectra (right) of the linker-cleaved (magenta) and tethered (black) fusion of SCD1-cyt b5. Almost identical SEC profile and optical spectra suggest the stable assembly between SCD1 and cyt b5. **c** Biphasic kinetics of NADH consumption by b5R with SCD1-cyt b5 fusion in the presence of substrate stearyl-CoA (red) compared to the slow linear decrease of NADH in the absence of substrate (orange). The absorbance of NADH at 340 nm ( $A_{340}$ ) was measured and the y axis is the normalized  $A_{340}$  against the initial values ( $A_{340,0}$ ). Excess NADH was used in the measurements. **d** The accelerated electron transfer between reduced cyt b5 and SCD1 in the SCD1-cyt b5 complex (brown) compared to that between the individual cyt b5 and SCD1 (yellow) and auto-oxidation of cyt b5 (orange). The Soret absorbance of reduced cyt b5 at 423 nm was monitored. One molar equivalent of NADH was added, which resulted in the initial rising phases of the fast electron transfer to cyt b5 via b5R. Rate constants ( $k$ ) are denoted as mean  $\pm$  SEM calculated from three independent repeats ( $n = 3$ ).

composed of lipids from liver polar extract or brain polar extract, it maintains the desaturation activity (Fig. 5e).

**Mutational studies of binary and ternary complexes.** Attempts to determine the structures of stable binary complexes of cyt b5 and SCD1, and cyt b5 and b5R, or the stable ternary complex of cyt b5, b5R and SCD1 by either X-ray crystallography or cryo-electron microscopy have not been successful. To gain further insight into the interactions between the TM domains, we made mutations to the TM region of cyt b5 and assessed the effect on the formation of the two stable binary complexes. We used the I-TASSER<sup>30</sup> and AlphaFold2<sup>31</sup> programs to generate a structural model of the TM helix of cyt b5 and b5R (Methods). We made single-point mutations to 10 consecutive residues, 119 – 128, of the predicted TM helix of cyt b5 in the context of either the SCD1-cyt b5-TEV chimera or cyt b5-b5R-TEV chimera. Small hydrophobic residues were replaced with a bulky Trp, and polar or large hydrophobic residues were replaced with Ala. Tryptophan substitution on TM domains was shown to weaken or disrupt dimerization of the CIC transporters<sup>32,33</sup>, although due to the amphipathic nature of its side chain, it may also shift the position of the TM helix. All but one mutants (residue 120) expressed, which allowed for a systematic perturbation of the stable binary complexes. After the fusion proteins were purified and cleaved by TEV protease, we examined the binary complexes by SEC. By monitoring the absorbance at 413 nm, where the binary complexes and monomeric cyt b5 have the same molar extinction coefficient, we were able to estimate the ratio of the heterodimer to monomer (Fig. 6 and Supplementary Fig. 4a, b).

In the SCD1-cyt b5 complex, the strongest effect was observed on M126A (~50% dissociation), with L121W, A122W, and L125W have a lower effect (~40% dissociation), and Y127A, R128A have the lowest effect (~10% dissociation) (Fig. 6a). In the cyt b5-b5R complex, A124W and R128A have the largest effect (~40% dissociation), with L121W and V123W, Y127A follows, and S119A, A122W, and M126A have the lowest effect (Fig. 6b). Overall, the effect of point mutations on the cyt b5-b5R complex tend to be more modest compared to these on the SCD1-cyt b5 complex. The varying degrees of complex dissociation in mutants were mapped onto the TM model of cyt b5 as shown in Fig. 6c, d. It seems that cyt b5 engages SCD1 or b5R using the opposite sides of its TM helix: the side of M126 interacts with SCD1, while the side of A124 and R128 with b5R (Fig. 6c, d). These results are consistent with the conclusion that the TM domains mediate the formation of stable binary and ternary complexes of SCD1, cyt b5, and b5R.

These results led us to propose a working model of an electron transport chain formed by a stable ternary complex of b5R, cyt b5, and SCD1 (Fig. 7). Cyt b5 and b5R form a stable binary complex that further interacts with SCD1 or other membrane-bound oxidoreductases to form a stable ternary complex. While the single TM helix of cyt b5 is sandwiched and thus immobilized between b5R and SCD1 in the stable ternary complex, its soluble domain is mobile and can alternate between interacting with b5R or SCD1 to relay electrons.

Soluble domains of SCD1, cyt b5, and b5R have clear complementary electrostatic charge distributions (Supplementary Fig. 5a). Soluble domains of SCD1 and b5R have positively

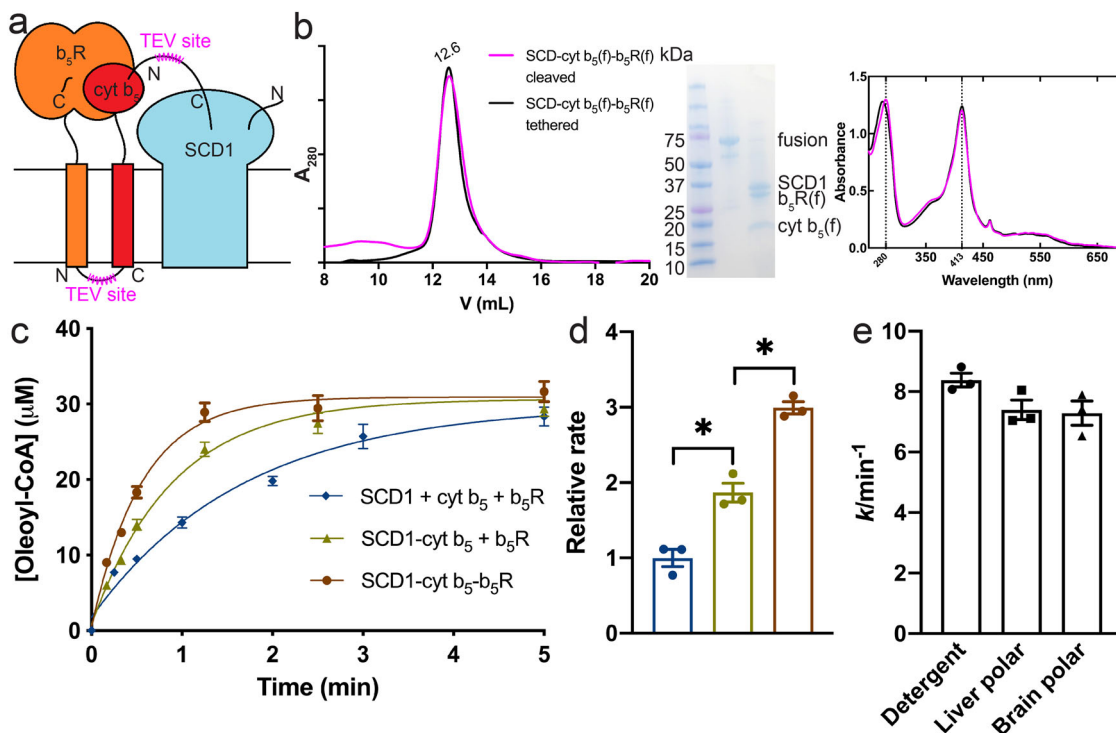


**Fig. 5** SCD1, full-length cyt  $b_5$ , and full-length  $b_5R$  can form a stable complex with faster electron transfer kinetics. **a** Schematic diagram of SCD1-cyt  $b_5$  fusion constructs. **b** SEC profile (left), SDS-PAGE image (inset), and UV-Vis spectra (right) of the linker-cleaved (magenta) and tethered (black) fusion of SCD1-cyt  $b_5$ - $b_5R$ . Almost identical SEC profile and optical spectra suggest the stable assembly among SCD1, cyt  $b_5$ , and  $b_5R$ . **c** Time courses of oleoyl-CoA production ( $n = 3$ ): individual SCD1, cyt  $b_5$  and  $b_5R$  (blue); the binary complex of SCD1-cyt  $b_5$  and individual  $b_5R$  (yellow); the ternary complex of SCD1-cyt  $b_5$ - $b_5R$  (brown). **d** Initial rate comparison among conditions in **c** ( $n = 3$ ). Asterisks indicate significant different ( $p < 0.05$ ) in pairwise  $t$  tests. **e** Initial rates of the SCD1-cyt  $b_5$ - $b_5R$  complex in detergent or liposomes. Error bars represent SEM from three independent repeats ( $n = 3$ ).

charged surfaces while that of cyt  $b_5$  has a negatively charged surface. Although in the context of a stable complex, electrostatic interactions no longer play a major role in the rate of electron transfer (Fig. 2c, d), charge-charge interactions could steer and align the donor-acceptor redox centers in the soluble domains. As a test of electrostatic interactions of the soluble domain of cyt  $b_5$  with either  $b_5R$  or SCD1, we mutated two charged residues, E43 and E49, on the surface of cyt  $b_5$  (Supplementary Fig. 5b, c) and measured their binding affinities to either  $b_5R$  or SCD1. The affinities to both  $b_5R$  and SCD1 decreased modestly in these mutants (Table 1 and Supplementary Fig. 6), suggesting that these residues are involved in interactions with both  $b_5R$  and SCD1.

## Discussion

In summary, we demonstrated that SCD1, cyt  $b_5$ , and  $b_5R$  form a stable ternary complex and that cyt  $b_5$  forms a stable binary complex with either  $b_5R$  or SCD1. The stable complexes are mediated by the TMs of the proteins, and the rates of electron transfer are significantly enhanced in the complexes. The facilitation of redox communication in binary and ternary complexes is demonstrated in both multiple and single turnover kinetic measurements for product formation and temporal changes of each redox center. The formation of a stable binary complex of  $b_5R$  and cyt  $b_5$  suggests it may interact with other downstream proteins as a single unit.

Cyt  $b_5$  is known to have a number of downstream partners, such as fatty acid desaturases and elongases, oxygenases, and cyt P450<sup>1,2</sup>, and this indicates that the soluble domain of cyt  $b_5$  is capable of interacting with different redox partners. Our study demonstrates that the TM domain of cyt  $b_5$  interacts with both the upstream partner ( $b_5R$ ) and at least one downstream partner,

SCD1, to form a stable ternary complex. We speculate that the TM of cyt  $b_5$  mediate the formation of stable complexes with other downstream enzymes.

Recent studies<sup>34–39</sup> using nuclear magnetic resonance and molecular dynamic simulation have shown interactions between TM helix of cyt  $b_5$  and that of cyt P450, an oxidoreductase with a single TM helix. The authors found that when both full-length cyt  $b_5$  and cyt P450 were incorporated into a single lipid nanodisc<sup>34</sup>, their TMs could interact and that the interactions facilitate electron transport between the soluble domains of cyt  $b_5$  and cyt P450<sup>37</sup>. Interestingly, a conserved motif on cyt  $b_5$  (L121–L125) that was thought to interact with cyt P450 in nanodiscs<sup>39</sup> is also identified in our study to mediate interactions with SCD1 and  $b_5R$ . Such conserved motif may serve to form hydrophobic packings with TM domains of various partners of cyt  $b_5$ .

Understanding the interactions of SCD1, cyt  $b_5$ , and  $b_5R$  and ultimately obtaining structures of the binary and ternary complexes in different redox states will help our understanding of SCD1 and other membrane-embedded oxidoreductases that rely on cyt  $b_5$  and  $b_5R$ . These interactions could be targeted by reagents that modulate electron transfers and enzymatic activities, and the biochemically stable complexes developed in this study could be used in high-throughput screens to identify such reagents.

## Methods

**DNA constructs.** The cDNAs of mouse SCD1 (UniProt ID: [P13516](#)), full-length cyt  $b_5$  (UniProt ID: [P56395](#)), and full-length  $b_5R$  (UniProt ID: [Q9DCN2](#)) were codon optimized and synthesized. Fusions of SCD1-cyt  $b_5$ , cyt  $b_5$ - $b_5R$ , SCD1-cyt  $b_5$ - $b_5R$  were generated by PCR. The linkers between each domain were either a TEV protease site (ENLYFQ/G) for the cleavable fusions or a flexible linker (GGSGGGSG) for the non-cleavable fusions. The SCD1 and SCD1-cyt  $b_5$  fusions were cloned into a pEG BacMam vector with a TEV protease site prepended to a

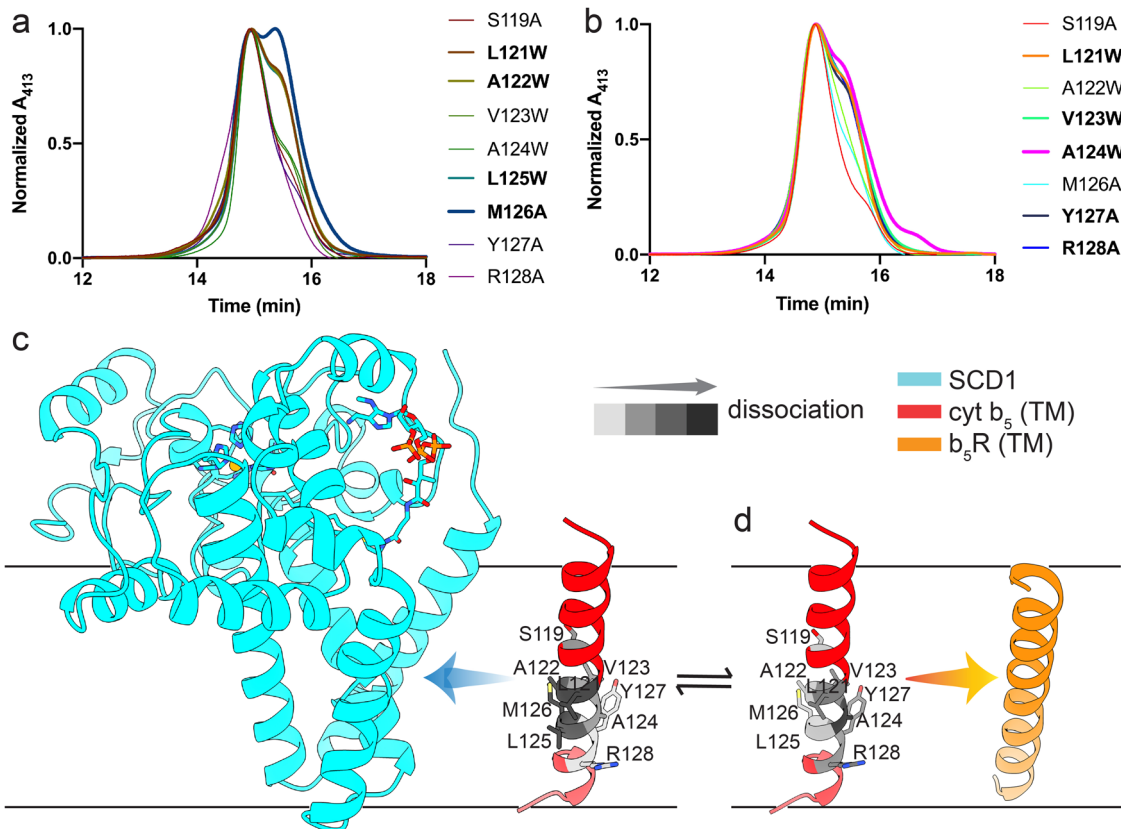


**Fig. 6 Mutations on the TM domains of SCD1, cyt b<sub>5</sub>, and b<sub>5</sub>R partially disrupt the stable complex assembly of the SCD1-cyt b<sub>5</sub> and the cyt b<sub>5</sub>-b<sub>5</sub>R.** SEC profiles of: **a** linker-cleaved SCD1-cyt b<sub>5</sub> complexes, and **b** linker-cleaved cyt b<sub>5</sub>-b<sub>5</sub>R complexes with mutations on TM domains. Residues on the TM helix of cyt b<sub>5</sub> were mutated to either an Ala from a polar or large hydrophobic residue or a bulky Trp from a small hydrophobic residue. The absorbance at 413 nm from the heme group in cyt b<sub>5</sub> was monitored. Mutants causing highest complex dissociation were highlighted. The model of complex assembly in: **c** SCD1 (cyan) and TM helix of cyt b<sub>5</sub> (red); and **d** TM helix of cyt b<sub>5</sub> (red) and b<sub>5</sub>R (orange). Residues important for complex assembly are shown as sidechain sticks and are colored per their degree of causing complex dissociation when mutated based on results in **a**, **b**. Darker color represents a larger effect on disrupting complex assembly. One-sided arrows indicate the side of the TM helix of cyt b<sub>5</sub> participating in the binary complex formation.

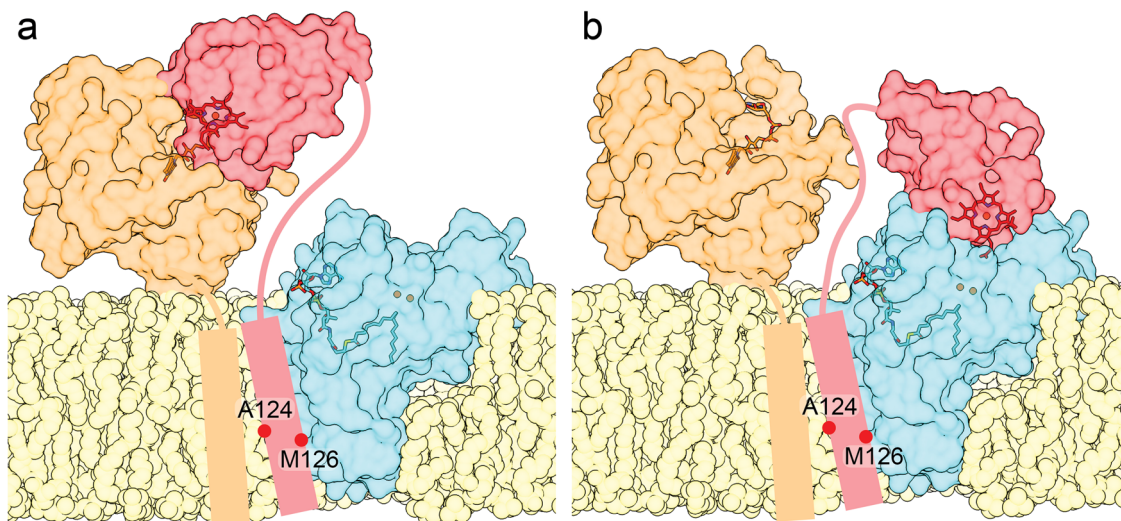


**Fig. 7 Model of the stable SCD1-cyt b<sub>5</sub>-b<sub>5</sub>R complex.** SCD1 (cyan), cyt b<sub>5</sub> (red), and b<sub>5</sub>R (orange) are shown as translucent surfaces highlighting the diiron center (orange sphere) and acyl-CoA (cyan stick) in SCD1, heme (deep red stick) in cyt b<sub>5</sub>, and FAD (brown stick) in b<sub>5</sub>R. SCD1 forms a complex with the TM helix of cyt b<sub>5</sub> and b<sub>5</sub>R in lipid bilayer (yellow). The relative positions of two residues on the TM helix of cyt b<sub>5</sub> are marked. A flexible linker connecting the soluble domain of cyt b<sub>5</sub> and b<sub>5</sub>R to their TM helix allows the transition of two states: **a** cyt b<sub>5</sub> receiving an electron from b<sub>5</sub>R; and **b** cyt b<sub>5</sub> delivering an electron to SCD1.



**Table 1 Binding affinities of soluble cyt b<sub>5</sub> to SCD1 or soluble b<sub>5</sub>R.**

K <sub>D</sub> (μM)	b <sub>5</sub> R	SCD1
cyt b <sub>5</sub> (WT)	2.71 ± 0.33	4.42 ± 1.77
cyt b <sub>5</sub> (E43A)	9.63 ± 0.97	11.2 ± 2.6
cyt b <sub>5</sub> (E49A)	8.45 ± 1.44	8.23 ± 2.49

K<sub>D</sub> values are denoted as mean ± SEM calculated from three measurements (n = 3). Sensorgrams are shown in Supplementary Fig. 6.

C-terminal GFP tag. Because the C-terminus of b<sub>5</sub>R ends on the interface of the FAD-binding domain and NADH-binding domain, no extra residue was introduced after the C-terminus of b<sub>5</sub>R domain to preserve its functional integrity. Therefore, SCD1-cyt b<sub>5</sub>-b<sub>5</sub>R was cloned into a pEG BacMam vector with an N-terminal GFP tag. For immunofluorescence imaging and coimmunoprecipitation assays, cyt b<sub>5</sub> and cyt b<sub>5</sub>-b<sub>5</sub>R with an N-terminal Myc tag, and b<sub>5</sub>R with an N-terminal HA tag were cloned into a pEG BacMam vector. For large-scale protein expression and purification, cyt b<sub>5</sub>, b<sub>5</sub>R, and cyt b<sub>5</sub>-b<sub>5</sub>R were cloned into a pFastBac Dual vector with an octa-histidine tag and a TEV protease site. For Octet binding assays, the soluble domains of cyt b<sub>5</sub> (4–89) and b<sub>5</sub>R (24–301) were cloned into a pET vector.

**Immunofluorescence imaging.** The HEK 293 S cells in *FreeStyle 293* media (Invitrogen/Thermo Fisher) supplemented with 2% fetal bovine serum (FBS; Sigma) were plated one day before transfection onto glass coverslips coated with poly-L-lysine in a 24-well plate. The cDNAs in pEG BacMam vectors were transfected into cells with Lipofectamine 2000 (Invitrogen/Thermo Fisher) per the manufacturer's instructions. About 24 h after transfection, cells were fixed with 2% paraformaldehyde for 10 min and then washed three times with phosphate-buffered saline (PBS). Cells were blocked and permeabilized with PBSAT (PBS + 1% bovine serum albumin, BSA + 0.1% Triton X-100) for 10 min. For cells expressing only GFP-tagged proteins, coverslips were washed three times with PBS and mounted onto glass slides with *ProLong Diamond* (Invitrogen/Thermo Fisher). For cells expressing Myc and/or HA tagged proteins, primary antibodies against Myc and/or HA tag diluted in PBSAT (1:200) were added and incubated for 45 min at room temperature (RT). Coverslips were washed three times with PBS before the incubation with Alexa Fluor 555 (for Myc tag) and/or Alexa Fluor 647 (for HA tag) conjugated secondary antibodies (Invitrogen/Thermo Fisher) diluted in PBSAT (1:2000) for 30 min at RT. Finally, coverslips were washed and mounted as mentioned before.

Confocal images were acquired with a Zeiss LSM-710 confocal microscope using a ×63 oil immersion objective (Zeiss, Plan-Apochromat ×63/1.4 Oil DIC M27) with *Immersionol 518 F* immersion oil (Zeiss). Alexa Fluor 647, Alexa Fluor 555, and GFP were detected sequentially with 633 nm HeNe laser, 561 nm diode-pumped solid-state laser, and 488 nm Argon laser. Crosstalk between the channels was avoided by adjusting emission regions. Single optical sections at a resolution of 1024 × 1024 pixels were acquired at two different zoom levels (×1.5 and ×4).

**Coimmunoprecipitation.** The HEK 293 S cells were plated one day before transfection in a 6-well plate. The pEG BacMam vectors containing target cDNAs were transfected with Lipofectamine 2000 (Invitrogen/Thermo Fisher) and incubated for 2 days. Cells on the plate were washed in PBS before scraping. Cell membranes were solubilized in lysis buffer (20 mM HEPES, pH 7.5, 150 mM NaCl, 10% glycerol) plus 0.2% Triton X-100 and Protease Inhibitor Cocktail (Roche) for 1 h at 4 °C. Cell debris were pelleted by centrifugation. The supernatants of cell lysate were incubated with either pre-equilibrated GFP nanobody-conjugated NHS-Activated Sepharose 4 Fast Flow Agarose (GE Healthcare) or *Pierce Protein A* Agarose (Invitrogen/Thermo Fisher) with rabbit anti-Myc antibodies for 30 min at 4 °C. The resins were extensively washed in lysis buffer plus 0.1% Triton X-100 within 5 min at 4 °C. In all, 4× Laemmli Sample Buffer (Bio-Rad) was added, and samples were run in SDS-PAGE without extra elution steps. Bands of target proteins were visualized by western blotting (Supplementary Fig. 7) with mouse anti-GFP (Invitrogen/Thermo Fisher) (1:1000), anti-Myc (1:500), and anti-HA (1:500) antibodies as primary antibodies and IRDye-800CW anti-mouse IgG (Licor) (1:5000) as the secondary antibody. Images were taken in an Odyssey infrared scanner (Licor).

**Large-scale expression and purification of proteins.** Expression of SCD1-containing proteins (SCD1, SCD1-cyt b<sub>5</sub>, and SCD1-cyt b<sub>5</sub>-b<sub>5</sub>R) was conducted in HEK 293 S cells using the BacMam system<sup>40</sup>. Baculoviruses were generated from pEGBacMam vectors with target cDNAs and amplified in Sf9 (*Spodoptera frugiperda*) cells. HEK 293 cells were maintained in *FreeStyle 293* media (Invitrogen/Thermo Fisher) supplemented with 2% FBS (Sigma) in a 37 °C incubator with 8% CO<sub>2</sub> atmosphere at 100 rpm. Baculoviruses after three passages (P3) were added to HEK 293 S cells at a density of 3 × 10<sup>6</sup> mL<sup>-1</sup> at a 7.5% v/v ratio and incubated

overnight before adding 10 mM sodium butyrate and lowering the temperature to 30 °C. Media were supplemented with transferrin and ferric chloride<sup>41</sup>, 0.5 mM δ-aminolevulinic acid and 100 μM riboflavin were added in media to enhance the biosynthesis of the heme and FAD group, respectively. Three days after infection, cells were harvested and resuspended in lysis buffer plus Protease Inhibitor Cocktail (Roche), 1 mM phenylmethylsulfonyl fluoride (PMSF), 5 mM MgCl<sub>2</sub> and DNase I. Solubilization of cell membranes was achieved by incubating with 30 mM n-dodecyl-β-D-Maltopyranoside (DDM, Anatrace) for 2 h at 4 °C under gentle agitation. Insoluble fractions were pelleted by centrifugation at 55,000 × g for 40 min. Target proteins in supernatants were captured by GFP nanobody resins during 1 h incubation at 4 °C. After washing the resins with 20 CV washing buffer (lysis buffer plus 1 mM DDM), the GFP-tagged proteins were released by TEV protease digestion during which the TEV protease site linkers in the cleavable fusions were also cleaved. The eluents were concentrated (Amicon 50-kDa cutoff, Millipore) and loaded onto a SEC column (Superdex 200 10/300 GL, GE Health Sciences) equilibrated with FPLC buffer (20 mM HEPES, pH 7.5, 150 mM NaCl, 1 mM DDM).

Expression of full-length cyt b<sub>5</sub>, full-length b<sub>5</sub>R, and cyt b<sub>5</sub>-b<sub>5</sub>R was conducted in High Five (*Trichoplusia ni*) cells using the Bac-to-Bac system. Baculoviruses were generated from pFastBac Dual vectors with target cDNAs. 1.5% v/v of P3 virus was added to cells at a density of 3 × 10<sup>6</sup> mL<sup>-1</sup>. The δ-aminolevulinic acid (Santa Cruz) and/or riboflavin (Sigma) were supplemented in media as mentioned above. Cells were harvested three days after infection. Membranes were solubilized by 30 mM DDM for 2 h at 4 °C under gentle agitation. Insoluble fractions were pelleted by centrifugation at 55,000 × g for 40 min. The His-tagged proteins in supernatants were captured by cobalt-based affinity resins (Talon, Clontech) during 1 h incubation at 4 °C. The resins were washed with 3 × 20 CV washing buffer plus imidazole up to 10 mM. The target proteins were released by TEV protease digestion. The eluents were concentrated (Amicon 50-kDa cutoff, Millipore) and loaded onto a SEC column (Superdex 200 10/300 GL, GE Health Sciences) equilibrated with FPLC buffer.

**UV-Vis spectroscopy and enzymatic assays.** UV-Vis spectra were recorded using a Hewlett-Packard 8453 diode-array spectrophotometer (Palo Alto, CA). The time courses of the NADH consumption at 340 nm and the spectral change of cyt b<sub>5</sub> heme at 423 nm were obtained with an Applied Photophysics (Leatherhead, UK) model SX-18MV stopped-flow instrument. The observed rates, k<sub>obs</sub>, were obtained by fitting the time courses to either 1- or 2-exponential functions.

Continuous turnover reactions of SCD1, the binary complex of SCD1-cyt b<sub>5</sub>, and the ternary complex of SCD1-cyt b<sub>5</sub>-b<sub>5</sub>R were performed in FPLC buffer. Briefly, 3 μM of: 1) SCD1 plus an equimolar of cyt b<sub>5</sub> and b<sub>5</sub>R; 2) SCD1-cyt b<sub>5</sub> plus an equimolar of b<sub>5</sub>R; and 3) SCD1-cyt b<sub>5</sub>-b<sub>5</sub>R in FPLC buffer were incubated with substrate stearoyl-CoA (Sigma). NADH was added to start the reaction. Aliquots of reaction mixtures were retrieved and quenched at different time points and analyzed in high-performance liquid chromatography (HPLC). The initial rates were calculated by linear fitting of time courses within 1 min after the reaction started.

**Liposome reconstitution and enzymatic assays.** Liver polar extract or brain polar extract lipids (Avanti) in chloroform were dried under a stream of Argon and then vacuumed for 1 h. Lipids were hydrated with FPLC buffer to a concentration of 10 mg/mL and sonicated to transparency. After three cycles of freeze-thaw, the empty liposomes were extruded through 400 nm filter membrane (NanoSizer™ Extruder, T&T Scientific Corporation) to homogeneity. Prior to the addition of protein, 0.11% (w/v) Triton X-100 (Sigma) was added to destabilize the liposome. SCD1-cyt b<sub>5</sub>-b<sub>5</sub>R complex was added at a protein to lipid ratio of 1:25 (w/w). Detergent was sequentially removed by a total amount of 240 mg per mL of semi-wet Bio-Beads SM-2 (BioRad).

Prior to enzymatic assays, 300 μM of stearoyl-CoA was added to the proteoliposomes. Unilaminar proteoliposomes were formed after three cycles of freeze-thaw and extrusions through 400 nm filter membranes as mentioned above. The desaturation reaction was triggered by the addition of 1 mM NADH. Reaction mixtures were quenched and analyzed by HPLC as described above.

**Size-exclusion chromatography of mutants.** Mutations on the TM domains of SCD1, cyt b<sub>5</sub>, and b<sub>5</sub>R were introduced to the constructs of linker-cleavable fusions of SCD1-cyt b<sub>5</sub> and cyt b<sub>5</sub>-b<sub>5</sub>R by QuikChange site-directed mutagenesis. All mutations were confirmed by sequencing. Expression and purification were done similarly to the wild-type (WT) fusions. Purified proteins were loaded onto a SEC column (SRE-10C SEC-300, Sepax) in an HPLC system with a diode-array detector (SPD-M20A, Shimadzu). Samples were run in FPLC buffer at a flow rate of 0.75 mL/min and monitored at 423 nm. Elution profiles were normalized to the peak corresponding to either the SCD1-cyt b<sub>5</sub> or the cyt b<sub>5</sub>-b<sub>5</sub>R complex for comparison.

**Modeling of single TM helices.** The TM regions of cyt b<sub>5</sub> and b<sub>5</sub>R were predicted by TMHMM server<sup>42</sup> and residue 108–134 of cyt b<sub>5</sub> and residue 1–28 of b<sub>5</sub>R were used to model a TM helix in I-TASSER server<sup>30</sup>. The helical models with the highest C-score were chosen and energy-minimized in CHARMM-GUI Membrane



Builder<sup>43–47</sup>. The were protonated at neutral pH and were embedded in a POPC bilayer.

**Octet biolayer interferometry.** Soluble cyt  $b_5$  and  $b_5R$  were expressed in BL21(DE3) cells with pET vectors containing target cDNA. Mutations in cyt  $b_5$  were introduced by QuikChange site-directed mutagenesis and were confirmed by sequencing. Expression procedures were adapted from established protocols<sup>48,49</sup>. Purification procedures were similar to those for full-length cyt  $b_5$  and  $b_5R$  as mentioned above.

Biolayer interferometry (BLI) assays were performed at 30 °C under constant shaking at 1000 rpm using an Octet system (FortéBio). The immobilization of ligand proteins on amine reactive second-generation (AR2G) biosensors (Sartorius) was done following the manufacturer's instructions. Briefly, biosensor tips were activated in 20 mM 1-ethyl-3-[3-dimethylaminopropyl]carbodiimide hydrochloride (EDC) and 10 mM N-hydroxysulfosuccinimide for 300 s. Then the tips were loaded with soluble cyt  $b_5$  at a concentration of 5 µg/mL in FPLC buffer for 600 s. The tips were quenched in FPLC buffer plus 1 M ethanolamine for 300 s. The tips with immobilized ligands were equilibrated in FPLC buffer plus 0.1% BSA to reduce non-specific binding. Then, they were transferred to wells of a concentration gradient (5, 2.5, and 1.25 µM) of analytes (soluble  $b_5R$  or SCD1) in buffer B for association and returned to the equilibration wells for dissociation. Binding curves were aligned and corrected with the channel of no analyte protein. The association and disassociation phases were fitted with a 1-exponential function to extract  $k_{on}$  and  $k_{off}$  of the binding, which were used to calculate dissociation constant  $K_D$ .

**Statistics and reproducibility.** No statistical method was used to determine sample size. Data used for statistical analyses were from at least three biological repeats. Statistical significances were indicated in the figures.

**Reporting summary.** Further information on research design is available in the Nature Research Reporting Summary linked to this article.

## Data availability

Source data (Supplementary Data 1) are provided along with the paper. Materials related to the fusion protein expression are available upon reasonable request to lead contact Ming Zhou (mzhou@bcm.edu).

Received: 10 March 2022; Accepted: 23 August 2022;

Published online: 12 September 2022

## References

- Schenkman, J. B. & Jansson, I. The many roles of cytochrome  $b_5$ . *Pharm. Ther.* **97**, 139–152 (2003).
- Elahian, F., Sepehrizadeh, Z., Moghimi, B. & Mirzaei, S. A. Human cytochrome  $b_5$  reductase: structure, function, and potential applications. *Crit. Rev. Biotechnol.* **34**, 134–143 (2014).
- Yamada, M. et al. Elucidations of the catalytic cycle of NADH-cytochrome  $b_5$  reductase by X-ray crystallography: new insights into regulation of efficient electron transfer. *J. Mol. Biol.* **425**, 4295–4306 (2013).
- Vergeres, G. & Waskell, L. Cytochrome  $b_5$ , its functions, structure and membrane topology. *Biochimie* **77**, 604–620 (1995).
- Ackerman, D. & Simon, M. C. Hypoxia, lipids, and cancer: surviving the harsh tumor microenvironment. *Trends Cell Biol.* **24**, 472–478 (2014).
- Theodoropoulos, P. C., Gonzales, S. S., Winterton, S. E. & Rodriguez-Navas, C. Discovery of tumor-specific irreversible inhibitors of stearoyl CoA desaturase. *Nat. Chem. Biol.* **12**, 218–225 (2016).
- Savino, A. M. et al. Metabolic adaptation of acute lymphoblastic leukemia to the central nervous system microenvironment is dependent on Stearoyl CoA desaturase. *Nat. Cancer* **1**, 998–1009 (2020).
- Oatman, N. et al. Mechanisms of stearoyl CoA desaturase inhibitor sensitivity and acquired resistance in cancer. *Sci. Adv.* **7**, <https://doi.org/10.1126/sciadv.abd7459> (2021).
- Fanning, S. et al. Lipidomic analysis of alpha-synuclein neurotoxicity identifies stearoyl CoA desaturase as a target for Parkinson treatment. *Mol. Cell* **73**, 1001–1014 e1008. (2019).
- Vincent, B. M. et al. Inhibiting stearoyl-CoA desaturase ameliorates alpha-synuclein cytotoxicity. *Cell Rep.* **25**, 2742–2754 e2731. (2018).
- Nuber, S. et al. A stearoyl-coenzyme a desaturase inhibitor prevents multiple parkinson disease phenotypes in alpha-synuclein mice. *Ann. Neurol.* **89**, 74–90 (2021).
- Paton, C. M. & Ntambi, J. M. Biochemical and physiological function of stearoyl-CoA desaturase. *Am. J. Physiol. Endocrinol. Metab.* **297**, <https://doi.org/10.1152/ajpendo.90897.2008> (2009).
- Aljohani, A. M., Syed, D. N. & Ntambi, J. M. Insights into stearoyl-CoA desaturase-1 regulation of systemic metabolism. *Trends Endocrinol. Metab.* **28**, 831–842 (2017).
- Gutiérrez-Juárez, R. et al. Critical role of stearoyl-CoA desaturase-1 (SCD1) in the onset of diet-induced hepatic insulin resistance. *J. Clin. Investig.* **116**, 1686–1695 (2006).
- Ntambi, J. M. et al. Loss of stearoyl-CoA desaturase-1 function protects mice against adiposity. *Proc. Natl Acad. Sci. USA* **99**, 11482–11486 (2002).
- Shirabe, K., Nagai, T., Yubisui, T. & Takeshita, M. Electrostatic interaction between NADH-cytochrome  $b_5$  reductase and cytochrome  $b_5$  studied by site-directed mutagenesis. *Biochim. Biophys. Acta.* **1384**, 16–22 (1998).
- Samhan-Arias, A. K. et al. Topography of human cytochrome  $b_5$ /cytochrome  $b_5$  reductase interacting domain and redox alterations upon complex formation. *Biochim. Biophys. Acta.* **1859**, 78–87 (2018).
- Dailey, H. A. & Strittmatter, P. Modification and identification of cytochrome  $b_5$  carboxyl groups involved in protein-protein interaction with cytochrome  $b_5$  reductase. *J. Biol. Chem.* **254**, 5388–5396 (1979).
- Strittmatter, P., Kittler, J. M., Coghill, J. E. & Ozols, J. Characterization of lysyl residues of NADH-cytochrome  $b_5$  reductase implicated in charge-pairing with active-site carboxyl residues of cytochrome  $b_5$  by site-directed mutagenesis of an expression vector for the flavoprotein. *J. Biol. Chem.* **267**, 2519–2523 (1992).
- Nishida, H. & Miki, K. Electrostatic properties deduced from refined structures of NADH-cytochrome  $b_5$  reductase and the other flavin-dependent reductases: pyridine nucleotide-binding and interaction with an electron-transfer partner. *Proteins* **26**, 32–41 (1996).
- Kawano, M., Shirabe, K., Nagai, T. & Takeshita, M. Role of carboxyl residues surrounding heme of human cytochrome  $b_5$  in the electrostatic interaction with NADH-cytochrome  $b_5$  reductase. *Biochem. Biophys. Res. Commun.* **245**, 666–669 (1998).
- Nagao, K., Murakami, A. & Umeda, M. Structure and function of  $\Delta 9$ -fatty acid desaturase. *Chem. Pharm. Bull.* **67**, 327–332 (2019).
- Rogers, M. J. & Strittmatter, P. The interaction of NADH-cytochrome  $b_5$  reductase and cytochrome  $b_5$  bound to egg lecithin liposomes. *J. Biol. Chem.* **250**, 5713–5718 (1975).
- Spatz, L. & Strittmatter, P. A form of reduced nicotinamide adenine dinucleotide-cytochrome  $b_5$  reductase containing both the catalytic site and an additional hydrophobic membrane-binding segment. *J. Biol. Chem.* **248**, 793–799 (1973).
- Man, W. C., Miyazaki, M., Chu, K. & Ntambi, J. Colocalization of SCD1 and DGAT2: implying preference for endogenous monounsaturated fatty acids in triglyceride synthesis. *J. Lipid Res.* **47**, 1928–1939 (2006).
- Steiner-Mordoch, S. et al. Parallel topology of genetically fused EmrE homodimers. *EMBO J.* **27**, 17–26 (2008).
- Nasie, I., Steiner-Mordoch, S., Gold, A. & Schuldiner, S. Topologically random insertion of EmrE supports a pathway for evolution of inverted repeats in ion-coupled transporters. *J. Biol. Chem.* **285**, 15234–15244 (2010).
- Stockbridge, R. B., Robertson, J. L., Kolmakova-Partensky, L. & Miller, C. A family of fluoride-specific ion channels with dual-topology architecture. *Elife* **2**, e01084 (2013).
- Meyer, T. E. et al. Transient kinetics of intracomplex electron transfer in the human cytochrome  $b_5$  reductase-cytochrome  $b_5$  system: NAD<sup>+</sup> modulates protein-protein binding and electron transfer. *Arch. Biochem. Biophys.* **318**, 457–464 (1995).
- Yang, J. & Zhang, Y. I-TASSER server: new development for protein structure and function predictions. *Nucleic Acids Res.* **43**, W174–W181 (2015).
- Jumper, J. et al. Highly accurate protein structure prediction with AlphaFold. *Nature* **596**, 583–589 (2021).
- Robertson, J. L., Kolmakova-Partensky, L. & Miller, C. Design, function and structure of a monomeric ClC transporter. *Nature* **468**, 844–847 (2010).
- Chadda, R. et al. The dimerization equilibrium of a ClC Cl<sup>-</sup>/H<sup>+</sup> antiporter in lipid bilayers. *Elife* **5**, <https://doi.org/10.7554/eLife.17438> (2016).
- Zhang, M. et al. Reconstitution of the Cyt $b_5$ -CytP450 Complex in Nanodiscs for Structural Studies using NMR Spectroscopy. *Angew. Chem. Int. Ed. Engl.* **55**, 4497–4499 (2016).
- Ahuja, S. et al. A model of the membrane-bound cytochrome  $b_5$ -cytochrome P450 complex from NMR and mutagenesis data. *J. Biol. Chem.* **288**, 22080–22095 (2013).
- Jerábek, P., Florián, J. & Martinek, V. Membrane-anchored cytochrome P450 1A2–cytochrome  $b_5$  complex features an X-shaped contact between antiparallel transmembrane helices. *Chem. Res. Toxicol.* **29**, 626–636 (2016).
- Zhang, M., Huang, R., Im, S. C., Waskell, L. & Ramamoorthy, A. Effects of membrane mimetics on cytochrome P450-cytochrome  $b_5$  interactions characterized by NMR spectroscopy. *J. Biol. Chem.* **290**, 12705–12718 (2015).

38. Yamamoto, K. et al. Dynamic interaction between membrane-bound full-length cytochrome P450 and cytochrome b<sub>5</sub> observed by solid-state NMR spectroscopy. *Sci. Rep.* **3**, 2538 (2013).
39. Yamamoto, K., Caporini, M. A., Im, S. C., Waskell, L. & Ramamoorthy, A. Transmembrane interactions of full-length mammalian bitopic cytochrome-P450-cytochrome-b<sub>5</sub> complex in lipid bilayers revealed by sensitivity-enhanced dynamic nuclear polarization solid-state NMR spectroscopy. *Sci. Rep.* **7**, 4116 (2017).
40. Goehring, A. et al. Screening and large-scale expression of membrane proteins in mammalian cells for structural studies. *Nat. Protoc.* **9**, 2574–2585 (2014).
41. Shen, J., Wu, G., Tsai, A. L. & Zhou, M. Structure and mechanism of a unique diiron center in mammalian stearyl-CoA desaturase. *J. Mol. Biol.* **432**, 5152–5161 (2020).
42. Krogh, A., Larsson, B., von Heijne, G. & Sonnhammer, E. L. Predicting transmembrane protein topology with a hidden Markov model: application to complete genomes. *J. Mol. Biol.* **305**, 567–580 (2001).
43. Jo, S., Kim, T. & Im, W. Automated builder and database of protein/membrane complexes for molecular dynamics simulations. *PLoS One* **2**, e880 (2007).
44. Wu, E. L. et al. CHARMM-GUI membrane builder toward realistic biological membrane simulations. *J. Comput. Chem.* **35**, 1997–2004 (2014).
45. Jo, S., Lim, J. B., Klauda, J. B. & Im, W. CHARMM-GUI membrane builder for mixed bilayers and its application to yeast membranes. *Biophys. J.* **97**, 50–58 (2009).
46. Jo, S., Kim, T., Iyer, V. G. & Im, W. CHARMM-GUI: a web-based graphical user interface for CHARMM. *J. Comput. Chem.* **29**, 1859–1865 (2008).
47. Lee, J. et al. CHARMM-GUI membrane builder for complex biological membrane simulations with glycolipids and lipoglycans. *J. Chem. Theory Comput.* **15**, 775–786 (2019).
48. Mulrooney, S. B. & Waskell, L. High-level expression in *Escherichia coli* and purification of the membrane-bound form of cytochrome b<sub>5</sub>. *Protein Expr. Purif.* **19**, 173–178 (2000).
49. Bando, S. et al. Structure of human erythrocyte NADH-cytochrome b<sub>5</sub> reductase. *Acta Crystallogr. Sect. D Biol. Crystallogr.* **60**, 1929–1934 (2004).

## Acknowledgements

We thank Dr. Theodore G Wensel for the access to the Zeiss confocal microscope and western blot-related materials; Dr. Melina A Agosto for the help with confocal microscopy and co-IP experiments; and Joshua I Rosario Sepulveda for the help with western blot. This work was supported by grants from NIH (DK122784 to M.Z. and A.T., HL086392 and GM098878 to M.Z.), and Cancer Prevention and Research Institute of Texas (R1223 to M.Z.).

## Author contributions

M.Z., A.T., J.S., and G.W. conceived the project. J.S. and G.W. conducted experiments. J.S. and M.Z. wrote the initial draft and all authors participated in revising the manuscript.

## Competing interests

The authors declare no competing interests.

## Additional information

**Supplementary information** The online version contains supplementary material available at <https://doi.org/10.1038/s42003-022-03882-z>.

**Correspondence** and requests for materials should be addressed to Ming Zhou.

**Peer review information** *Communications Biology* thanks Kanwal Kayastha, Emma Waters, Dirk Schneider, and the other, anonymous, reviewer(s) for their contribution to the peer review of this work. Primary Handling Editor: Gene Chong.

**Reprints and permission information** is available at <http://www.nature.com/reprints>

**Publisher's note** Springer Nature remains neutral with regard to jurisdictional claims in published maps and institutional affiliations.



**Open Access** This article is licensed under a Creative Commons Attribution 4.0 International License, which permits use, sharing, adaptation, distribution and reproduction in any medium or format, as long as you give appropriate credit to the original author(s) and the source, provide a link to the Creative Commons license, and indicate if changes were made. The images or other third party material in this article are included in the article's Creative Commons license, unless indicated otherwise in a credit line to the material. If material is not included in the article's Creative Commons license and your intended use is not permitted by statutory regulation or exceeds the permitted use, you will need to obtain permission directly from the copyright holder. To view a copy of this license, visit <http://creativecommons.org/licenses/by/4.0/>.

© The Author(s) 2022